Journal of Materials Chemistry C



PAPER



Cite this: *J. Mater. Chem. C*, 2020, **8**, 8135

Received 18th February 2020, Accepted 7th May 2020

DOI: 10.1039/d0tc00830c

rsc.li/materials-c

From spin-crossover to single molecule magnetism: tuning magnetic properties of Co(II) bis-ferrocenylterpy cations *via* supramolecular interactions with organocyanide radical anions†

Haomiao Xie, Kuduva R. Vignesh, D. Xuan Zhang And Kim R. Dunbar **D**

TCNQ (7,7,8,8-tetracyanoquinodimethane) anion-radical derivatives were used to fine tune the magnetic properties of the $[Co^{II}(Fctp)_2]^{2+}$ (Fctp = 4'-(2-ferrocenyl)-2,2':6'2"-terpyridine) cation in the solid state. The cocrystallization of $[Co^{II}(Fctp)_2]^{2+}$ with $TCNQ^{\bullet-}$ yielded the two pseudo-polymorphic products $[Co^{II}(Fctp)_2]$ ($TCNQ)_2$) (1) and $[Co^{II}(Fctp)_2]$ ($TCNQ)_2$ -MeCN (2) whereas the analogous reaction with $TCNQF^{\bullet-}$ (TCNQF) (1) and $TCNQF^{\bullet-}$ (TCNQF) (2) whereas the analogous reaction with $TCNQF^{\bullet-}$ (TCNQF) (3). Compound 1 exhibits slow relaxation of magnetization under an applied $TCNQF^{\bullet-}$ (TCNQF) (3). Compound 1 exhibits slow relaxation of magnetization under an applied $TCNQF^{\bullet-}$ ($TCNQF^{\bullet-}$) and $TCNQF^{\bullet-}$ ($TCNQF^{\bullet-}$) and $TCNQF^{\bullet-}$ anion-radical derivatives.

Introduction

Molecule-based materials that exhibit magnetic bistability are promising candidates for the design of new generations of electronic and magnetic devices, two important categories of which are spin-crossover (SCO) compounds^{1–3} and single-molecule magnets (SMM).^{4–7} The up/down spin states or the differences in magnetic moments between high-spin states and low-spin states provide the basic units for data storage and/or quantum computing.

Supramolecular interactions are well known for their capacity to tune SCO^{8–10} and SMM^{11–16} behaviour. Our particular interest is the study of supramolecular interactions of Co(II) SCO moieties with anions and solvent molecules.^{17,18} In general, the low-spin (L.S.) Co^{II} state is favoured as the ground state in bis(terpy) derivatives due to the strong ligand field of the terpyridine ligand.^{19–21} The SCO phenomenon in [Co^{II}(terpy)₂]²⁺ cations can be mediated by geometric restrictions and supramolecular interactions, the effects of which lower the energy gap between H.S. and L.S. states. In addition to these intrinsic effects in the solid state, there are several rare examples of compounds with either SCO or SMM properties whose properties can be interconverted *via* ligand or crystal field modifications or light

Department of Chemistry, Texas A&M University, College Station, Texas 77842-3012, USA. E-mail: dunbar@chem.tamu.edu irradiation.^{21–28} Recently, Wang and co-workers reported that the presence or absence of water molecules in the interstices of a crystal triggers a single-crystal to single-crystal transition that induces a switching between SCO and SMM behavior.²⁹ These interesting findings notwithstanding, difficulties in predicting the position and intermolecular interactions of solvents in a crystal renders this approach untenable for the rational design of materials with tunable properties.

The introduction of supramolecular interactions between magnetic cations and counter anions constitutes a more promising strategy than random packing of solvent molecules for tuning solid-state structures and magnetic functionalities. Recently, Hayami and coworkers 10 achieved tuning of the SCO behaviour of the $[Fe^{II}(qnal)_2]^+$ cation by introducing aromatic counterions, but structure–function relationships were not possible given that larger conjugated aromatic anions altered not only the $\pi \cdots \pi$ interactions between the anion and the SCO metal cation but also the overall geometric parameters.

In the current study, the co-crystallization of $[Co^{II}(Fctp)_2]^{2+}$ cations (Fctp = 4'-ferrocenyl-2,2':6',2"-terpyridine) that contain redox-active pendant ferrocenyl groups with $TCNQ^{\bullet}$ and $TCNQF^{\bullet}$ radical anions (TCNQ = 7,7,8,8-tetracyanoquinodimethane, TCNQF = 2-fluoro-7,7,8,8-tetracyanoquinodimethane) led to the isolation of supramolecular assemblies of the magnetic cations and the tunable organocyanide anions. Introduction of the ferrocenyl pendant group changes the solid state architecture with respect to the geometry of the cation moiety and facilitates $\pi \cdots \pi$

[†] Electronic supplementary information (ESI) available. CCDC 1911576–1911578 and 1964462. For ESI and crystallographic data in CIF or other electronic format see DOI: 10.1039/d0tc00830c

interactions between the ferrocenyl and TCNQ/TCNQF moieties. The advantages of introducing TCNQ* or TCNQF* are (1) π -conjugation enables $\pi \cdot \cdot \cdot \pi$ interactions with cationic moieties that contain aromatic groups; (2) the fluorine substituent on TCNQF^{• –} tunes the frontier orbital energies as well as its electron accepting ability and introduces a dipole moment which engenders dipole-dipole interactions and (3) similar van der Waals radii of fluorine (1.47 Å) and hydrogen atoms (1.20 Å) $^{30-32}$ allows for the preservation of the solid state structure with minimum perturbations form steric effects. The three compounds [Co^{II}(Fctp)₂](TCNQ)₂ (1), [Co^{II}(Fctp)₂](TCNQ)₂·MeCN, (2), and [Co^{II}(Fctp)₂](TCNQF)₂·MeCN, (3), were obtained as crystals from co-crystallization of [Co^{II}(Fctp)₂]²⁺ cations with TCNQ^{• –} and TCNQF^{• –} radical anions. The paramagnetic moiety, $[Co^{II}(Fctp)_2]^{2+}$, in 1 exhibits SMM behaviour under an applied field whereas the isomorphs 2 and 3 exhibit non-identical SCO behaviour. Structural, magnetic and computational studies were performed to probe the structureproperty relationships in the solid state.

Experiment

Synthetic procedures

LiTCNQ³³ and LiTCNQF^{34,35} salts were prepared according to reported methods. All experiments were performed under a N_2 atmosphere. Solvents were purified by distillation under N_2 .

Synthesis of the Fctp ligand

The synthesis of Fctp has been reported in the literature. 36 A modified one-pot synthesis was used for the ligand synthesis.³⁷ A quantity of NaOH (0.8 g, 20 mmol) was suspended in 15 mL of polyethylene glycol 300 at 0 °C and 2-acetylpyridine (2.42 g, 20 mmol) was added at 0 °C with stirring for 10 minutes after which time 10-methyl-3-formylphenothiazine (2.41 g, 10 mmol) was added to form a dark red solution. Stirring at 0 °C was continued for an additional 2 hours after which time the temperature was gradually increased to room temperature. An aliquot of NH₃·H₂O (30%, 30 mL) was added and the mixture was refluxed for 12 hours. After the solution had cooled to room temperature, 50 mL of water was added and the resulting yellow-brown precipitate was collected by filtration, washed with 50 mL of hot ethanol and dried in air. The yield was 1.27 g (2.8 mmol, 28%) of orange powder. ¹H-NMR (300 MHz, CDCl₃): δ (in ppm) 8.75 (d, 2H), 8.66 (dt, 2H), 8.52 (d, 2H), 7.88 (td, 2H), 7.36 (ddd, 2H), 5.02 (t, 2H), 4.47 (t, 2H), 4.10 (s, 5H). IR (KBr, cm⁻¹): 1602.9 (s), 1581.6 (s), 1566.2 (m), 1548.8 (m), 1465.9 (s), 1408.0 (s), 1386.8 (m), 1103.3 (m), 819.7 (s), 800.5 (s), 787.0 (s), 731.0 (s), 669.3 (s), 657.7 (m), 621.1 (m).

Synthesis of [Co^{II}(Fctp)₂](PF₆)₂

The salt $[Co^{II}(Fctp)_2](PF_6)_2$ was prepared by a modified literature method. A sample of $Co(OAc)_2$ - $4H_2O$ (0.5 mmol, 125 mg) was dissolved in 5 mL of methanol and Fctp (1 mmol, 419 mg) in 4 mL CHCl₃ was added gradually which led to the formation of a dark purple solution. The mixture was stirred at room temperature for 30 minutes and 508 mg of a dark purple powder was obtained by adding an aqueous solution of KPF₆ (278 mg in 10 mL H₂O).

The product was collected and dried in air; 85.3% yield. IR (KBr, cm⁻¹): 1610.6 (m), 1543.0 (m), 1496.8 (m), 1471.7 (m), 1433.1 (m), 1251.8 (m), 1107.1 (m), 1031.9 (m), 829.4 (vs), 790.8 (s), 746.5 (m), 671.2 (m), 655.8 (m).

Synthesis of [Co^{II}(Fctp)₂](TCNQ)₂ and [Co^{II}(Fctp)₂](TCNQ)₂·MeCN

The salts $[Co^{II}(Fctp)_2](PF_6)_2$ (0.05 mmol, 59 mg) and LiTCNQF (0.1 mmol, 21 mg) were separately dissolved in 5 mL of MeCN/ MeOH (1:1, v/v). The two solutions were layered in a 20 mL test tube for one week. During this time, two distinct phases of crystals formed with different colours and morphologies. A manual separation of the two phases gave 23 mg of purple block crystals (1, [Co^{II}(Fctp)₂](TCNQ)₂) and 8 mg of intensely coloured blue platelets (2, [Co^{II}(Fctp)₂](TCNQ)₂·MeCN). IR of 1 (KBr, cm⁻¹): 3097.7 (w), 2169.9 (s), 2148.7 (s), 1583.6 (s), 1543.0 (m), 1504.5 (s), 1471.7 (m), 1433.1 (s), 1350.2 (s), 1176.6 (s), 1012.6 (m), 825.5 (s), 787.0 (s). Elemental analysis of 1: calculated (%): C (68.27), H (3.56), N (15.06); found: C (67.99), H (3.55), N (15.15). IR of 2 (KBr, cm⁻¹): 3076.5 (w), 2173.8 (s), 2150.6 (s), 1602.8 (m), 1568.1 (s), 1504.5 (s), 1433.1 (m), 1361.7 (s), 1170.8 (s), 1004.9 (m), 825.5 (s), 788.9 (s), 746.4 (m), 669.3 (m), 574.8 (m). Elemental analysis of 2: calculated (%): C (67.69), H (3.68), N (15.65); found: C (67.71), H (3.74), N (15.53).

Synthesis of [Co^{II}(Fctp)₂](TCNQF)₂·MeCN

Samples of $[Co^{II}(Fctp)_2](PF_6)_2$ (0.05 mmol, 59 mg) and LiTCNQF (0.1 mmol, 23 mg) were dissolved in 5 mL of MeCN/MeOH (1:1, v/v) and layered in a 20 mL test tube for one week. A 32 mg quantity of a pure phase in the form of intensely coloured blue platelet crystals (3, $[Co^{II}(Fctp)_2](TCNQF)_2 \cdot MeCN)$ were obtained. IR (KBr, cm⁻¹): 3078.4 (w), 2179.6 (s), 2160.3 (s), 1599.0 (s), 1570.0 (m), 1543.0 (m), 1494.8 (s), 1433.1 (m), 1381.0 (s), 1357.9 (s), 1253.7 (m), 1188.2 (m), 1016.5 (m), 825.5 (m), 788.9 (s), 746.4 (m), 729.1 (m), 669.3 (m), 574.8 (m). Elemental analysis: calculated (%): C (66.20), H (3.44), N (15.24); found: C (66.08), H (3.40), N (15.15).

Single crystal X-ray crystallography

Single-crystal diffraction data of **1** were collected at 100 K with the synchrotron radiation source (λ = 0.41328 Å) at the Chem-MatCars beamline 15-ID-B at the Advanced Photon Source (APS), Argonne National Laboratories. Crystals of **2** and **3** were collected at 120 K on a Bruker D8 Quest diffractometer equipped with a microfocus MoK α radiation source (λ = 0.71073 Å) with a I μ s CMOS detector. The data sets were recorded by the ϕ -scan and ϕ -scan methods and integrated with Bruker APEX 3 software package. Absorption corrections were performed in the SADABS-2016/2 (Bruker, 2016/2) package. Solution and refinement of the crystal structures was carried out using the SHELXT³⁸ and SHELXL³⁹ programs and the graphical interface Olex2.⁴⁰

Powder X-ray diffraction

Powder X-ray diffraction data were collected on a Bruker D8 powder X-ray diffractometer at room temperature with Cu X-ray radiation to verify the phase purity of the bulk products. Powder diffraction patterns were simulated from single crystal X-ray structural data by using Mercury CSD 2.0.

Magnetic measurements

A Quantum Design MPMS-XL SQUID instrument was used for magnetic measurements over the temperature range of 1.8-300 K and in the field range of 0-7 T. The ac measurements were performed with a 2 Oe measuring field using frequencies from 1 to 1000 Hz. The diamagnetic contributions of sample holders and diamagnetic contributions of atoms were corrected by using a calibrated empty sample holder and Pascal's constants.

Computational details

Ab initio CASSCF (Complete Active Space Self-Consistent Field) calculations were performed to compute the ZFS (D) of the Co^{II}, ion for 1 using the ORCA 3.0 suite of programs. 41 The BP86 functionals were employed along with scalar relativistic ZORA Hamiltonians and ZORA-def2-TZVP basis sets for the metal ions and the first coordination sphere and def2-SVP was used for the remainder of the atoms. The RI approximation with secondary TZV/J coulombic fitting basis sets were used along with increased integration grids (Grid 5 in ORCA convention). The tight SCF convergence was used throughout the calculations $(1 \times 10^{-8} E_{\rm h})$. The SOC contributions in the *ab initio* framework were obtained using second-order perturbation theory as well as by employing the effective Hamiltonian approach which enables calculations of all matrix elements to be made numerically with the anisotropic spin Hamiltonian from the ab initio energies and wave functions. The state average-CASSCF (Complete Active Space Self-Consistent Field) method was used to compute the ZFS. The active space comprises seven active electrons in five active d-orbitals (d⁷ system; CAS (7,5)) for the Co^{II} ion. With this active space, 10 quartet and 40 doublet states were computed for the Co^{II} ion by the configuration interaction procedure. ⁴² The d-orbital ordering was plotted using 'LOEWDIN-energies' from the ORCA output that contains each root contribution and the corresponding electronic arrangement along with their plausible transition energies. The Effective Hamiltonian from the CASSCF calculation provides the calculated D and E parameters with their "Individual contribution to the *D*-tensor". For each contribution the program predicts the plausible transition energies between the d-orbitals and those D values compared with the LOEWDIN energies. In order to understand the SCO behaviour of 2, DFT calculations were performed using the TPSSh functional^{43,44} with Alhrich^{45,46} triple-ζ basis set as implemented in the Gaussian 09 suite of programs.

DFT calculations were performed to investigate the intermolecular interactions between [Co^{II}(Fctp)]²⁺ and (TCNQ)₂²⁻/ (TCNQF)₂²⁻ using the Gaussian 09 program.⁴⁷ A long-range corrected functional with dispersion corrections, ωB97x-D, 48 was employed for the single point energy calculation with cc-pVTZ basis sets for metal ions and 6-311++G** basis sets for the other atoms.

Result and discussion

X-ray crystallographic studies

For the reaction between [Co^{II}(Fctp)₂](PF₆)₂ and LiTCNQ, two types of pseudo-polymorphic products with different colours and morphologies, 1 and 2, were obtained. The major product

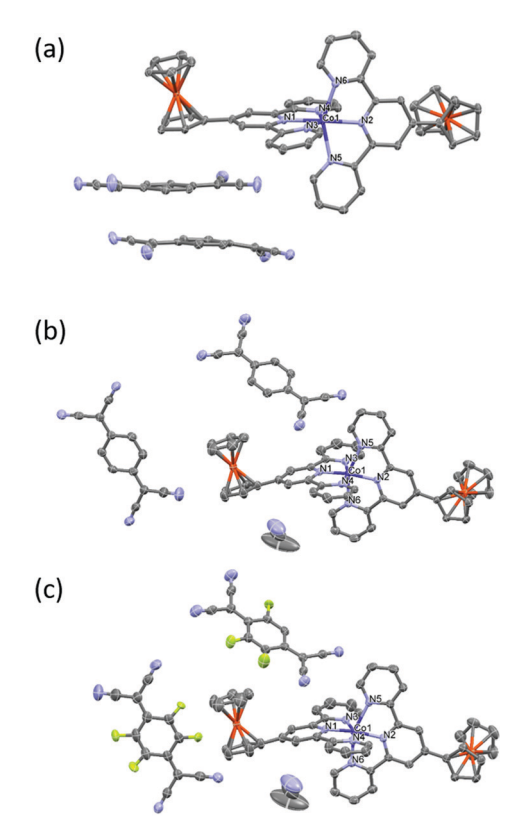


Fig. 1 The asymmetric units in the crystal structures of (a) [Co^{II}(Fctp)₂](TCNQ)₂ (1), (b) [Co^{II}(Fctp)₂](TCNQ)₂·MeCN (2) and (c) [Co^{II}(Fctp)₂](TCNQF)₂·MeCN (3) with thermal ellipsoids drawn at the 70% probability level. The fluorine atoms are disordered in TCNQF and the hydrogen atoms are omitted for the sake of clarity. Color code: carbon: grey; nitrogen: blue; cobalt: purple; iron: orange; fluorine: yellow.

is the purple block phase 1 ([Co^{II}(Fctp)₂] (TCNQ)₂, phase-I) and the minor one is the dark blue platelet phase of 2, ([Co^{II}(Fctp)₂] (TCNQ)₂·MeCN, phase-II). The structures of 1 (at 100 K) and 2 (at 120 K) were elucidated by single-crystal X-ray diffraction methods (Fig. 1(a), (b) and Table S1, ESI†). The Co(II) ions in both phases are six-coordinate with nitrogen atoms from two Fctp ligands, but the Co-N distances are significantly different in 1 and 2 as evidenced by the data compiled in Table 1. In phase 1, the cobalt centre is in a compressed octahedral geometry and exhibits relatively long, and nearly equal, axial Co1-N1 (2.045(2) Å) and Co1-N2 (2.054(2) Å) distances which fall into the range of highspin Co^{II} species.²¹ In contrast, the phase-II structure exhibits shorter axial Co-N bond distances of 1.877(2) Å for Co1-N1 and 1.936(2) Å for Co1-N2, an indication that the Co(II) centre is in the low-spin state. 17,21,49 Continuous shape measure (CShMs) analysis was performed with SHAPE 2.150 and the results are summarized in Table S2 (ESI†). The smallest deviation values for Co(II) centres in 1 (5.283) and 2 (2.771), are found for the octahedral geometry. Compound 1 exhibits a larger deviation from the octahedral geometry than 2, which is in accord with reported values of high-spin and SCO Co(II)-bis(terpy) compounds.²⁹

A single crystal phase, [Co^{II}(Fctp)₂](TCNQF)₂·MeCN phase-II (3), was obtained when the reaction was performed with LiTCNQF. Compounds 2 and 3 are isomorphs as evidenced by the unit cell

Table 1 Co-N bond distances in 1, 2 and 3

Bond length/Å	$1([\mathrm{Co^{II}}(\mathrm{Fctp})_2](\mathrm{TCNQ})_2)$	$2([\mathrm{Co^{II}(Fctp)_2}](\mathrm{TCNQ})_2 \cdot \mathrm{MeCN})$	$3([Co^{II}(Fctp)_2](TCNQF)_2 \cdot MeCN)$
Co1-N1	2.045(2)	1.877(2)	1.873(2)
Co1-N2	2.054(2)	1.936(2)	1.944(2)
Co1-N3	2.195(2)	1.987(2)	1.978(2)
Co1-N4	2.161(2)	1.998(2)	1.990(2)
Co1-N5	2.153(2)	2.157(2)	2.162(2)
Co1-N6	2.155(2)	2.136(2)	2.138(2)

dimensions and contents (at 120 K, Table S1 and Fig. S1, ESI†). The Co–N bond distances in 3 slightly deviate from the ones in 2 but all are within the range for L.S. $Co(\pi)$ compounds. The fluorine substituent on $TCNQF^{\bullet-}$ in 3 disordered and was modelled with partial occupancies that sum to 1 for each $TCNQF^{\bullet-}$ asymmetric unit.

Supramolecular interactions, especially $\pi \cdots \pi$ contacts, play an important role in organizing the solid-state structures of the new materials. In the case of 1, the interplanar distance for the two distinct TCNQ^{• –} radicals is 2.911 Å in 1 (Fig. S2(a), ESI[†]), much shorter than the sum of the van der Waals radii of two carbon atoms (3.40 Å). This short contact is an indication that the TCNQ• radical anion pairs exist as antiferromagnetically coupled π -dimers⁵¹ which is also confirmed by the magnetic measurements of the zinc analogue (1') of 1. The ferrocenyl group also engages in a short contact (3.108 Å) with a TCNQ* radical anion which serves to constrain the geometry of the [Co^{II}(Fctp)₂]²⁺ cation. Two other short contacts that involve pyridyl groups on the Fctp ligand are also observed with relatively longer distances (3.316 Å for ferrocenyl···pyridyl and 3.402 Å for TCNQ···pyridyl) (Fig. S2(a), ESI†). These short contacts propagate a one-dimensional chain along the a axis of the unit cell (Fig. S2(b), ESI \dagger).

The packing patterns for 2 and 3 are different from 1 in that two types of TCNQ $^{\bullet}$ or TCNQF $^{\bullet}$ radical anions are present, one of which is similar to the π -dimer in 1 with interplanar distances of 2.998 Å for 2 and 3.007 Å for 3 respectively (Fig. S3, ESI †) The other type of radical is not dimerized⁴⁹ and exhibits interplanar distances of 3.529 Å for 2 and 3.543 Å for 3 respectively, which are longer than the sum of van der Waals radii. No similar face-to-face short contacts between the ferrocenyl group and TCNQ $^{\bullet}$ or TCNQF $^{\bullet}$ radical anion are observed for 2 and 3. Powder X-ray diffraction measurements at room temperature were compared with the simulations from the single-crystal structures (Fig. S4, ESI †). Resolvable peaks from the experiments were found in the simulated corresponding ones. Slight shifts of the peaks is due to the thermal expansion effect and the gradual SCO effects.⁵²

Magnetic properties

Temperature-dependent magnetic susceptibility measurements of **1**, **2** and **3** were performed under a 0.1 T DC field over the temperature range of 1.8–300 K. The phase purities of **1**, **2** and **3** (Fig. S4, ESI†) were verified by powder X-ray diffraction. The isomorphic zinc analogue (1') of **1** was also synthesized and characterized to evaluate the magnetic contribution from TCNQ $^{\bullet-}$ (Section S7 in ESI†). The room temperature χT value of **1** is 3.00 emu K mol $^{-1}$ which is higher than the expected value for a spin-only S = 3/2 (1.88 emu K mol $^{-1}$) ion due to

spin-orbit coupling. The decrease of χT value at low temperature is attributed to zero-field splitting effects. The magnetic behaviour at ~ 10 K (Fig. 2(a)) indicates the possibility of a negative D due to the splitting of first-order spin-orbit coupling in the low-lying orbital doublet.⁵³ This was further investigated by ab initio calculations (see the theoretical calculation section). Magnetization data at 1.8 K and reduced magnetization data from 1.8 to 5 K were also collected (Fig. S5(c), ESI†). The Hamiltonian in eqn (1) was used to simultaneously fit the temperature-dependent (Fig. 2(a)) and field-dependent (Fig. 2(b)) static magnetic susceptibility data. The H, β , D, E, g symbols are the magnetic field strength, the Bohr magneton, the axial, rhombic magnetic anisotropy and g tensor, respectively. The best fit gives $D = -57.0 \text{ cm}^{-1}$, $E = -17.9 \text{ cm}^{-1}$, $g_x = 2.07$, $g_y = 2.20$ and $g_z = 3.06$. The *D* value from fitting was comparable to the reported value for high-spin Co(II) bis-terpyridine compounds.²⁹ A reasonable unique fit was obtained by using these parameters; the shapes of fielddependent magnetization curves indicate strong dependence on the anisotropy of g tensor at low temperature.

$$\hat{H} = D \left[\hat{\mathbf{S}}_z^2 - \frac{1}{3} \hat{\mathbf{S}} \left(\hat{\mathbf{S}} + 1 \right) \right] + E \left(\hat{\mathbf{S}}_x^2 - \hat{\mathbf{S}}_y^2 \right) + g \beta H \hat{\mathbf{S}}$$
 (1)

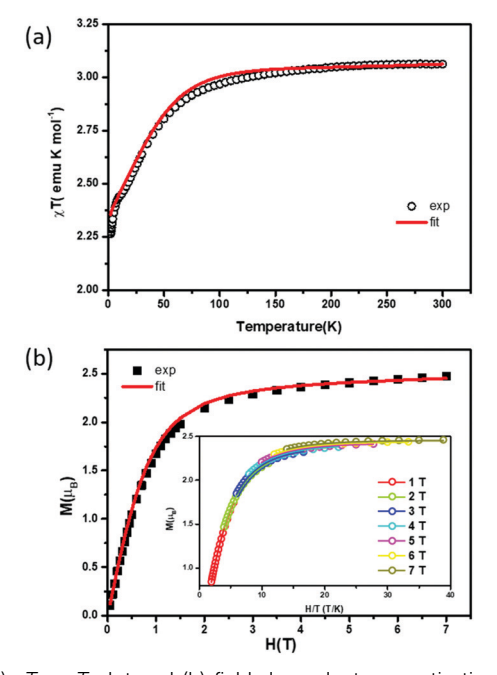


Fig. 2 (a) χT vs. T plot and (b) field-dependent magnetization curve at 1.8 K for compound **1**. (Inset: Reduced magnetization plots from 1–7 T). The solid lines are the best fit from the Hamiltonian in eqn (1).

An AC study of compound 1 was performed under 0-6000 Oe external DC fields at 1.8 K. No out-of-phase signals were observed under 0 Oe which is due to fast quantum tunnelling of the magnetization (QTM). The relaxation times (τ) under different DC fields were extracted from fittings of Cole-Cole plots (Table S1, ESI†). The τ value increases as the field increases from 250 Oe to 1750 Oe and then decreases up to 6000 Oe. Two relaxation processes, OTM and direct spin-phonon relaxation, were taken into consideration to fit the field-dependence of τ^{-1} (eqn (2) where A, B₁, B_2 are coefficients and H is the magnetic field strength).

$$\tau^{-1} = \frac{B_1}{1 + B_2 H^2} + AH^4 T + \text{const.}$$
 (2)

The least square fitting yielded $A = 7.77 \times 10^3 \text{ T}^{-4} \text{ K}^{-1} \text{ s}^{-1}$, $B_1 = 0.97 \times 10^3 \text{ s}^{-1}$ and $B_2 = 3.39 \times 10^2 \text{ T}^{-2}$. The individual components of the contributions from different relaxation processes are shown in Fig. 3(a), from which it can be ascertained that the effect of QTM is suppressed as the field increases. Conversely, the contribution from direct spin-phonon relaxation increases as the field strength increases. The τ^{-1} reaches its minimum at approximately $H_{dc} = 1750$ Oe.

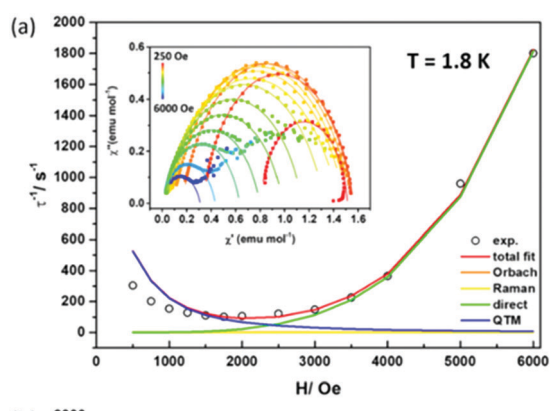
The temperature dependence of the relaxation time was also investigated under two different DC fields (500 Oe and 1750 Oe). The out-of-phase signals and Cole-Cole plots are shown in Fig. 4 and Fig. S6, S7 (ESI†). Two additional terms, an Orbach process and a Raman process, were introduced to model the temperature dependence of τ^{-1} :

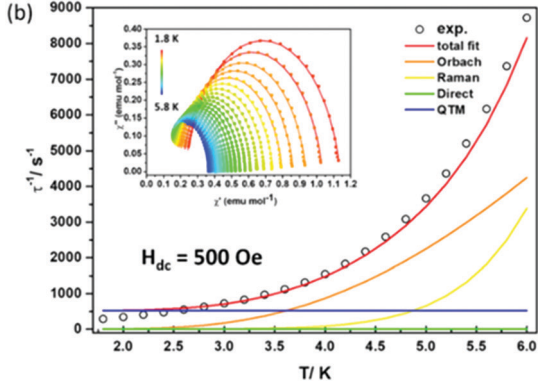
$$\tau^{-1} = \tau_0^{-1} e^{\frac{U_{\text{eff}}}{Tk_B}} + CT^n + AH^4T + \frac{B_1}{1 + B_2H^2}$$
 (3)

where C and n are Raman components and U_{eff} and k_{B} are the effective energy barrier and Boltzmann constant, respectively.

The best fit yields: $U_{\rm eff} = 19.1 \text{ K}$, $\tau_0 = 9.8 \times 10^{-6} \text{ s}$, $C = 3.4 \times 10^{-6} \text{ m}$ $10^{-4} \text{ K}^{-9} \text{ s}^{-1}$, n = 9 (Fig. 3(b) and (c)) The U_{eff} and τ_0 values are comparable to reported field-induced SMMs with six-coordinate Co^{II} centers.⁵⁴ The Raman components C and n are in the range expected for a Kramers ion (n = 6-9 and C < 0.1). The QTM process under 1750 Oe is well suppressed compared to a field of 500 Oe. At low temperatures, the contribution to τ^{-1} is primarily from an Orbach process under a 1750 Oe DC field whereas the contribution from the Raman process is insignificant at low temperature but increases rapidly as the temperature increases.

The γT values for 2 (Fig. 5) increase from 0.748 emu K mol⁻¹ at 2 K, which corresponds to two S = 1/2 spin centres ($\chi T =$ 0.375 for S = 1/2, g = 2.00), to 1.96 emu mol⁻¹ K⁻¹ at 300 K. The contribution to χT at 2 K is from low-spin $\mathrm{Co^{II}}$ and the nondimerized TCNQ radical which is in good agreement with the observed crystal structure. The high-spin state of Co^{II} in 2 is not fully populated at 300 K compared to that of 1 for which the χT value is ~ 3 emu mol⁻¹ K⁻¹ at 300 K. Similar spincrossover behaviour for 3 was observed. The χT value at 2 K is 0.848 emu K mol⁻¹, slightly higher than the value for 2, and increases more rapidly than 2 to reach a value of 3.20 emu K mol⁻¹ at 300 K. These results indicate that the L.S. to H.S. transition of the $[Co^{II}(Fctp)_2]^{2+}$ cation is facilitated in 3 compared to 2. The incomplete spin-state transition of 3 at





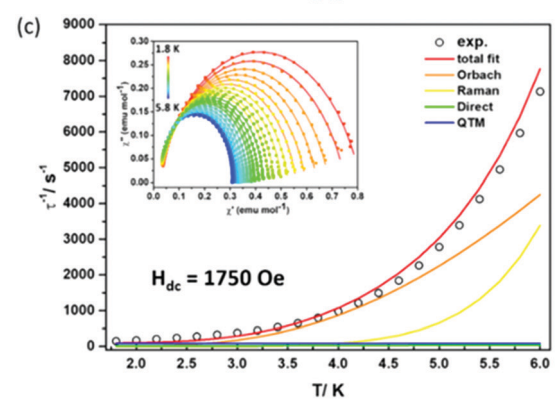


Fig. 3 (a) Magnetic field dependence, (b) and (c) temperature dependence of 1 with the best fits by using eqn (2) and (3). The insets are Cole-Cole plots (solid squares) with fits (solid lines).

low temperature is attributed to the geometric constraints of the crystal lattice and coordination sphere and/or supramolecular interactions. ^{49,57–59} The fitting of the $\chi T \nu s$. T curves for 2 and 3 is discussed in detail in Section S7 in the ESI.† 60,61 The best fit (Fig. S11(c), ESI†) led to values of $\Delta H = 8.69 \text{ kJ mol}^{-1}$, $\Delta S =$ 25.8 J K⁻¹ mol⁻¹ for 2 which exhibits a $T_{1/2}$ of 336 K and $\Delta H =$ 3.12 kJ mol⁻¹, $\Delta S = 13.8$ J K⁻¹ mol⁻¹ for 3 with a $T_{1/2}$ of 226 K. The magnitude of ΔH and ΔS for 2 and 3 are comparable to the reported Co^{II}-bisterpy SCO compounds. ^{29,61} Given that 2 and 3 are isostructural, the only variance that can account for the difference in SCO behaviour is the presence of TCNQ* versus the TCNQF* radical anions. As expected, no out-of-phase signals were observed for 2 and 3 at 1.8 K under external DC fields from 0 to 6000 Oe which is consistent with an S = 1/2 ground state with no energy barrier between $M_s = \pm 1/2$ states.

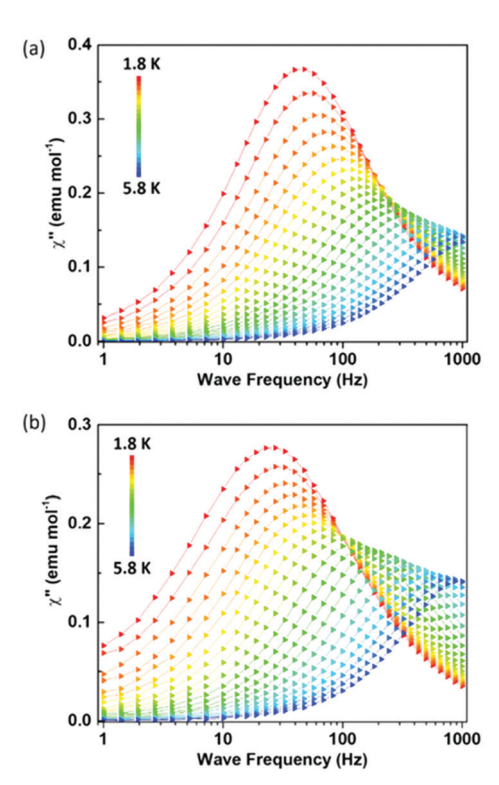


Fig. 4 Out-of-phase signal of compound **1** under (a) 500 Oe and (b) 1750 applied dc field.

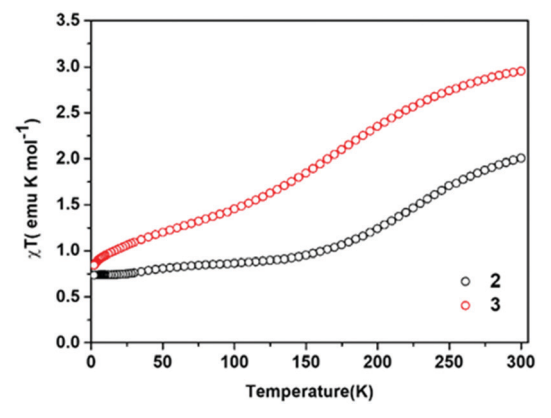


Fig. 5 χT vs. T plot of SCO complexes 2 (black circles) and 3 (red circles).

Theoretical calculations

Ab initio CASSCF calculations were carried out to probe the origin and sign of the observed D values of Co^{II} ion in 1. Computed g_x , g_y and g_z values along with the transition energies of the first four excited states and their contributions to the D value for 1 are listed in Table 2. Calculations yielded a g value of 2.36, in good agreement with the experimentally determined g value of 2.44.

The CASSCF computed splitting of the d orbitals for the Co^{II} ion in **1** is depicted in Fig. 6. The results indicate that the first transition of the β spin occurs between the d_{xz} and d_{yz} orbitals with the same $|\pm m_1|$ level which leads to a negative *D* value. ^{62,63} This low energy transition (\sim 1013 cm⁻¹) contributes a large

Table 2 CASSCF computed D, E/D and g_x , g_y and g_z values, transition energies (cm⁻¹) and contributions to D value from the first four excited states for **1**

D (in cm ⁻¹) and E/D	g_x, g_y, g_z	Excited state	Energy	D contribution
-59.9 and 0.15	2.07, 2.22, 2.80	First Second Third Fourth	2624.4 7075.8	8.4

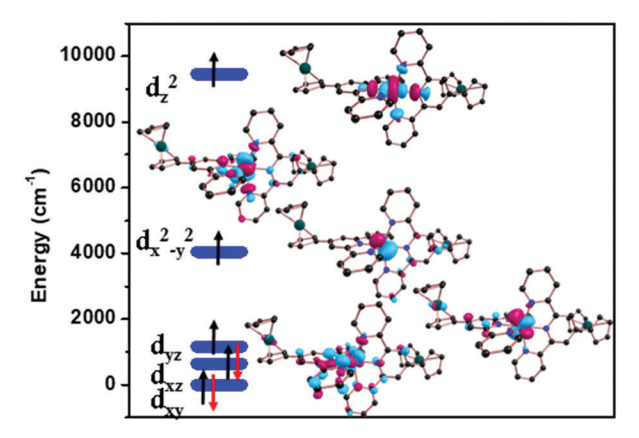


Fig. 6 CASSCF-computed d-orbital ordering for the Co(\shortparallel) ion in 1. Spin-up (black) and spin-down (red) arrows represent α and β electrons. The pink and blue regions indicate the positive and negative signs of wave functions respectively.

D value ($-70.2 \, \mathrm{cm}^{-1}$). The second transition occurs between d_{xy} and d_{yz} orbitals with different $|\pm m_{\mathrm{l}}|$ levels which contributes a positive D ($+8.4 \, \mathrm{cm}^{-1}$) to the total D value. Small contributions ($-3.9 \, \mathrm{cm}^{-1}$) from the third and fourth transition ($+1.1 \, \mathrm{cm}^{-1}$) do not affect the overall negative D value in a significant manner. The CASSCF computed D value of $-59.9 \, \mathrm{cm}^{-1}$ is in excellent agreement with the experimental D value of $-57.2 \, \mathrm{cm}^{-1}$ for 1.

DFT calculations using the TPSSh functional (see computational details) were undertaken to unravel details of the spin-crossover features observed for 2.64 Computed structural parameters for 2 along with its X-ray structural parameters are summarized in Table S7 (ESI†). The structural parameters of the optimized structures are generally in good agreement with the X-ray structural parameters. The optimized low-spin (S = 1/2) structure in particular closely resembles the X-ray structure. The computed energies of 2 are provided in Table S8 (ESI†). For 2, the Low-Spin (LS) state was found to be the ground state which is consistent with experimental data; the High-Spin (HS) state lies at 13.6 kJ mol^{-1} for 2. It is noted that, although the average error of TPSSh calculation results for such SCO systems was reported to be ~ 15.5 kJ mol⁻¹ (or 3.70 kcal mol⁻¹) which is close to our result here, the predicted LS-HS energy difference is in the expected range of 0 to 25 kJ mol⁻¹ for the observation of spin-crossover behavior in 2 which confirms the spin-crossover features. 65,66

DFT calculations with the $\omega B97x$ -D functional were also performed to investigate the intermolecular interactions between the high-spin $[\text{Co}^{II}(\text{Fctp})_2]^{2+}$ cation and the $(\text{TCNQ})_2^{2-}/(\text{TCNQF})_2^{2-}$ π -dimers with the phase-I structure. Phase-I is the structure that

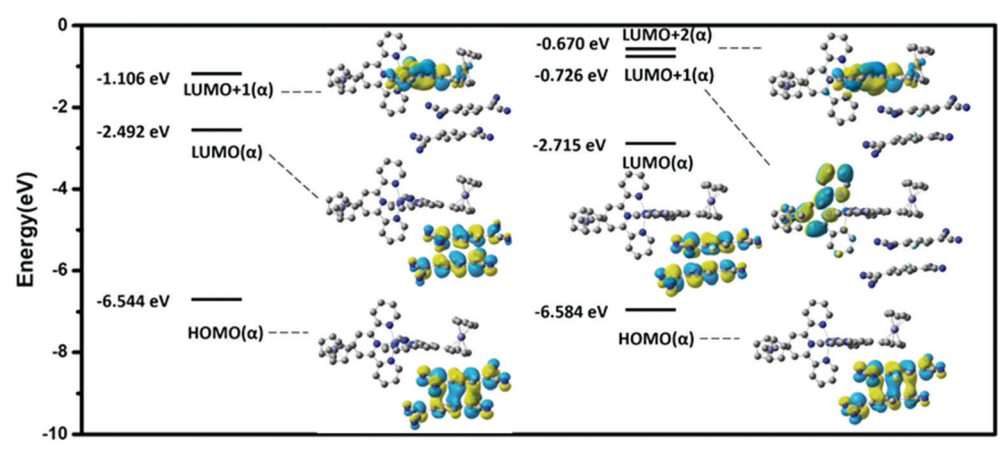


Fig. 7 DFT-computed frontier molecular orbitals energy diagram of {[Co(Fctp)₂](TCNQ)₂} and {[Co(Fctp)₇](TCNQF)₇} complexes. The orbital surfaces were plotted with 0.02 isovalue. The yellow and blue regions indicate the positive and negative signs of wave functions respectively.

involves $\pi \cdot \cdot \cdot \pi$ stacking between ferrocenyl group and TCNQ. The comparison was made to address why the TCNQF does not favor the phase-I structure. The energy diagram of the frontier molecular orbitals for {[Co(Fctp)₂](TCNQ)₂} (c1) and {[Co(Fctp)₂](TCNQF)₂} (c2) complexes is depicted in Fig. 7. The HOMO (E = -6.544 eV for c1 and -6.584 eV for c2) and LUMO (E = -2.492 eV for c1 and -2.715 eV for c2) levels for both compounds are based on the $(TCNQ)_2^{2-}/(TCNQF)_2^{2-}$ π -dimer bonding and antibonding orbitals (Fig. S13, ESI†). The HOMO and LUMO energies are slightly lower for c2 due to the electron withdrawing effect of the fluorine substituent on TCNQF $^{\bullet-}$. The LUMO+1 orbital (E = -1.106 eV) of c1 is mainly based on the π -antibonding orbital on the terpyridine ligand and the d orbital on the ferrocenyl group attached to it. The LUMO+2 orbital of c2 is nearly identical to the LUMO+1 of c1 but lies at higher energy (-0.670 eV). In contrast, the LUMO+1 orbital of c2 has similar characteristics to the orbital compositions of LUMO+2 but is located on the terpyridine ligand that is distal from the $(TCNQF)_2^{2-}$ π -dimer. The destabilization of the LUMO+1 and LUMO+2 orbitals of c2 is caused by an increase of coulombic repulsion due to the presence of the fluorine atom on (TCNQF)₂². Thus, the energy gap of the (TCNQ)₂²⁻/(TCNQF)₂²⁻ charge transfer to [Co^{II}(Fctp)₂]²⁻ that involves the $\pi \cdots \pi$ interactions, $\Delta E_{d \rightarrow a}$, increases from 5.438 eV to 5.914 eV when TCNQ[•] is replaced by TCNQF[•].

Discussion

The fact that reactions between [Co^{II}(Fctp)₂]²⁺ and TCNQ^{•-}/ TCNQF^{• –} produce compounds with different magnetic properties presents an ideal case for probing the role of supramolecular interactions. For the TCNQ* case, two phases were obtained, a major product, 1 (phase-I), with SMM properties and a minor product, 2 (phase-II) with SCO behaviour. In contrast, only one compound, 3 (phase-II), was isolated under the same experimental conditions. These findings indicate that phase-I is more favoured when TCNQ* is used as a counterion and phase-II is more favoured for the TCNQF*- derivative.

An important finding in this work is the isolation of compound 1 which exists in the H.S. state. Typically, Co^{II} complexes with terpyridine ligands exist in the L.S. ground state with the H.S. state as excited state 19-21 and, in fact, there are only a few examples of Co(II)-bis(terpyridine)-type compounds that exist in the H.S. state and which exhibit SMM behaviour. 29,67,68 Thus phase-II products should be favoured in all cases. The increase in energy required to stabilize $[Co^{II}(Fetp)_2]^{2+}$ in the high-spin state in compound 1 (phase-I) is provided by the supramolecular interactions between the ferrocenyl groups and TCNO[•]. As mentioned above, a significant difference in the structures of phase-I and phase-II is the presence of short contacts between the ferrocenyl group on $[Co^{II}(Fctp)_2]^{2+}$ with the $TCNQ^{\bullet -}$ π -dimer (~ 3.108 Å, Fig. S2, ESI†) in the former material, which is quite short and falls into the category of $\pi \cdots \pi$ interactions.⁶⁹

The energy contributions from the $\pi \cdot \cdot \cdot \pi$ interactions can be decomposed into the sum of electrostatic ($\Delta E_{\rm electrostat}$), Pauli $(\Delta E_{\mathrm{Pauli}})$, and orbital interaction $(\Delta E_{\mathrm{orb}})$ terms.⁷⁰ Given the evidence of destabilization of the LUMO+1 and LUMO+2 orbitals of **c2** from the DFT calculations, the $\Delta E_{\text{electrostat}}$ and ΔE_{Pauli} terms are augmented by the increase in electron density on (TCNQF)₂² as compared to $(TCNQ)_2^{2-}$ which renders the $\pi \cdots \pi$ interaction unfavourable. The $\Delta E_{\rm orb}$ term, the absolute value of which is inversely related to $\Delta E_{d\rightarrow a}$ of the donor-acceptor pair involved in the $\pi \cdots \pi$ stacking, ^{70,71} also plays an important role in stabilizing the high-spin Co(II) ion in the phase-I structure. The energy diagram obtained from the calculations (Fig. 7), indicates that the $\Delta E_{d\rightarrow a}$ value increases from 5.438 eV to 5.914 eV due to the fluorine substituent. The energy of the donor HOMO is lowered by the electron withdrawing effect of the fluorine and the LUMO+1 on the acceptor is raised in energy by coulombic repulsion from the electron density on the fluorine substituent; therefore the $\Delta E_{\rm orb}$ term is more negative for the TCNQ case. Given these findings, the $\pi \cdots \pi$ interactions are weaker for the $\{[Co(Fctp)_2](TCNQF)_2\}$ material than for {[Co(Fctp)₂](TCNQ)₂}. As a result, the phase-I structure is more favoured with TCNQ*- and less favoured for TCNQF^{• -} owing to the differences in $\pi \cdots \pi$ interaction strength between the [Co^{II}(Fctp)₂]²⁺ cations and TCNQ^{• –}/TCNQF anions.

Compounds 2 and 3 are isomorphs with the only difference being the fluorine substituent on the TCNQ $^{\bullet-}$ radical anion. The disparity in SCO behaviour between 2 and 3 is attributed to the differences in polarities of TCNQ $^{\bullet-}$ and TCNQF $^{\bullet-}$. The asymmetrically substituted TCNQF $^{\bullet-}$ radical anion in 3 (Fig. S12, ESI †) is disordered in the structure with uneven site occupencies which indicates that the interaction of dipole moments between $[\text{Co}^{\text{II}}(\text{Fctp})_2]^{2^+}$ and TCNQF $^{\bullet-}$ are significant at the crystallization temperature of \sim 298 K. The enthalpy change, ΔH , decreases from 8.69 kJ mol $^{-1}$ for 2 to 3.12 kJ mol $^{-1}$ for 3. The changes in ΔH may be caused by the electric dipolar interactions in the solid-state which reduce the energy difference between the high-spin state and low-spin state in phase-II structures.

The entropy changes, ΔS , are also critical for determining the $T_{1/2}$ values for the SCO phases in this study. The ΔS decreases from 25.8 J K^{-1} mol⁻¹ for 2 to 13.8 J K^{-1} mol⁻¹ for 3. Similar trends for Fe(II) SCO complexes have been observed in solution phases with different solvent polarities. The contributions to ΔS are mainly from two sources, the electronic contribution, ΔS_{el} , and vibrational contribution, ΔS_{vib} . The major variation in ΔS for 2 and 3 is ascribed to the differences in $\Delta S_{\rm vib}$ since $\Delta S_{\rm el}$ $(\sim 5.76 \text{ J K}^{-1} \text{ mol}^{-1})^{61}$ is the same for Co(II) in 2 and 3. Experimental and theoretical calculations support the conclusion that the major contribution to ΔS_{vib} in SCO systems is due to metal-ligand vibrations that corresponding to Jahn-Teller distortions associated with the spin-state transition, ^{73–79} which also induce dipole moment changes of the six-coordinate Co^{II} ion in 2 and 3 (Fig. S14, ESI†). Thus, considering the non-zero dipole moment of TCNQF*-, the electric dipole interactions between [Co^{II}(Fctp)₂]²⁺ and TCNQF^{• –} are responsible for the differences in ΔS for 2 and 3 which leads to the distinct SCO behaviour of these materials.

Conclusions

Three new compounds [Co^{II}(Fctp)₂] (TCNQ)₂ (1), [Co^{II}(Fctp)₂] (TCNQ)₂·MeCN (2) and [Co^{II}(Fctp)₂] (TCNQF)₂·MeCN, (3), were prepared and found to exhibit diverse magnetic properties owing to the presence of the radical anion TCNQ* versus TCNQF[•]. Two pseudopolymophic products, 1 as the major product and 2 as the minor product, were obtained from the same reaction. Compound 1 exhibits SMM behaviour under applied DC fields with an effective energy barrier $U_{\rm eff}$ of 19.1 K and a pre-exponential factor of τ_0 = 9.8 \times 10⁻⁶ s, whereas 2 exhibits SCO behaviour. The use of TCNQF^{• -} instead of TCNQ^{• -} exclusively leads to the isolation of 3 which is isostructural with 2. Both 2 and 3 exhibit SCO behaviour but with different transition temperatures, $T_{1/2} = 336$ K for 2 and $T_{1/2}$ = 226 K for 3. The collective results of single crystal X-ray studies, theoretical calculations, and thermodynamic parameters indicate that the preference for different phases and SCO behaviour is related to supramolecular interactions between [Co^{II}(Fctp)₂]²⁺, and the assemblies of the radical anions TCNQ* and TCNQF*. These results demonstrate that redox-active organic anions are useful tools for introducing supramolecular interactions and for fine-tuning the magnetic properties of open-shell metal cations by taking advantage

of conjugation for $\pi \cdots \pi$ interactions, the presence of tunable frontier orbital energies, and the polarity of the organic moieties.

Conflicts of interest

There are no conflicts to declare.

Acknowledgements

We gratefully acknowledge funding from the National Science Foundation under CHE-1808779 and the Robert A. Welch Foundation under Grant A-1449 for summer support for HX. The X-ray diffractometer and SQUID magnetometer used in this research were purchased with funds provided by the Texas A&M University Vice President of Research. We thank the HPRC and LMS at Texas A&M University for providing software and computing resources. The ChemMatCARS Sector 15 is principally supported by the Divisions of Chemistry (CHE) and Materials Research (DMR), National Science Foundation, under grant number NSF/CHE-1834750. Use of the Advanced Photon Source, an Office of Science User Facility operated for the U.S. Department of Energy (DOE) Office of Science by Argonne National Laboratory, is supported by the U.S. DOE under Contract No. DE-AC02-06CH11357.

Notes and references

- 1 O. Kahn and C. J. Martinez, Science, 1998, 279, 44-48.
- 2 K. S. Kumar and M. Ruben, Coord. Chem. Rev., 2017, 346, 176-205.
- 3 G. Molnar, S. Rat, L. Salmon, W. Nicolazzi and A. Bousseksou, *Adv. Mater.*, 2018, **30**, 1703862.
- 4 E. Moreno-Pineda, C. Godfrin, F. Balestro, W. Wernsdorfer and M. Ruben, *Chem. Soc. Rev.*, 2018, 47, 501–513.
- 5 L. Bogani and W. Wernsdorfer, *Nat. Mater.*, 2008, 7, 179–186.
- 6 S. Thiele, F. Balestro, R. Ballou, S. Klyatskaya, M. Ruben and W. Wernsdorfer, *Science*, 2014, 344, 1135–1138.
- 7 A. Gaita-Arino, F. Luis, S. Hill and E. Coronado, *Nat. Chem.*, 2019, **11**, 301–309.
- 8 J. Tao, R. J. Wei, R. B. Huang and L. S. Zheng, *Chem. Soc. Rev.*, 2012, **41**, 703–737.
- 9 K. Takahashi, T. Sakurai, W. M. Zhang, S. Okubo, H. Ohta, T. Yamamoto, Y. Einaga and H. Mori, *Inorganics*, 2017, 5, 54.
- 10 A. Tsukiashi, M. Nakaya, F. Kobayashi, R. Ohtani, M. Nakamura, J. M. Harrowfield, Y. Kim and S. Hayami, *Inorg. Chem.*, 2018, 57, 2834–2842.
- 11 W. Wernsdorfer, N. Aliaga-Alcalde, D. N. Hendrickson and G. Christou, *Nature*, 2002, **416**, 406–409.
- 12 T. N. Nguyen, W. Wernsdorfer, K. A. Abboud and G. Christou, J. Am. Chem. Soc., 2011, 133, 20688–20691.
- 13 A. M. Mowson, T. N. Nguyen, K. A. Abboud and G. Christou, *Inorg. Chem.*, 2013, **52**, 12320–12322.
- 14 T. N. Nguyen, W. Wernsdorfer, M. Shiddiq, K. A. Abboud, S. Hill and G. Christou, *Chem. Sci.*, 2016, 7, 1156–1173.
- 15 D. I. Alexandropoulos, B. S. Dolinar, K. R. Vignesh and K. R. Dunbar, *J. Am. Chem. Soc.*, 2017, **139**, 11040–11043.

- 16 B. S. Dolinar, D. I. Alexandropoulos, K. R. Vignesh, T. James and K. R. Dunbar, J. Am. Chem. Soc., 2018, 140, 908-911.
- 17 X. Zhang, Z. X. Wang, H. Xie, M. X. Li, T. J. Woods and K. R. Dunbar, Chem. Sci., 2016, 7, 1569-1574.
- 18 X. Zhang, H. M. Xie, M. Ballesteros-Rivas, Z. X. Wang and K. R. Dunbar, J. Mater. Chem. C, 2015, 3, 9292-9298.
- 19 H. S. Scott, C. J. Gartshore, S. X. Guo, B. Moubaraki, A. M. Bond, S. R. Batten and K. S. Murray, Dalton Trans., 2014, 43, 15212-15220.
- 20 K. Takami, R. Ohtani, M. Nakamura, T. Kurogi, M. Sugimoto, L. F. Lindoy and S. Hayami, Dalton Trans., 2015, 44, 18354-18359.
- 21 S. Hayami, Y. Komatsu, T. Shimizu, H. Kamihata and Y. N. Lee, Coord. Chem. Rev., 2011, 255, 1981-1990.
- 22 S. Mossin, B. L. Tran, D. Adhikari, M. Pink, F. W. Heinemann, J. Sutter, R. K. Szilagyi, K. Meyer and D. J. Mindiola, J. Am. Chem. Soc., 2012, 134, 13651-13661.
- 23 R. Ababei, C. Pichon, O. Roubeau, Y. G. Li, N. Brefuel, L. Buisson, P. Guionneau, C. Mathoniere and R. Clerac, J. Am. Chem. Soc., 2013, 135, 14840-14853.
- 24 X. Feng, C. Mathoniere, R. Jeon Ie, M. Rouzieres, A. Ozarowski, M. L. Aubrey, M. I. Gonzalez, R. Clerac and J. R. Long, J. Am. Chem. Soc., 2013, 135, 15880-15884.
- 25 I. A. Gass, S. Tewary, A. Nafady, N. F. Chilton, C. J. Gartshore, M. Asadi, D. W. Lupton, B. Moubaraki, A. M. Bond, J. F. Boas, S. X. Guo, G. Rajaraman and K. S. Murray, Inorg. Chem., 2013, 52, 7557-7572.
- 26 H. H. Cui, J. Wang, X. T. Chen and Z. L. Xue, Chem. Commun., 2017, 53, 9304-9307.
- 27 D. Shao, L. D. Deng, L. Shi, D. Q. Wu, X. Q. Wei, S. R. Yang and X. Y. Wang, Eur. J. Inorg. Chem., 2017, 3862-3867.
- 28 L. Chen, J. Song, W. Zhao, G. Yi, Z. Zhou, A. Yuan, Y. Song, Z. Wang and Z. W. Ouyang, Dalton Trans., 2018, 47, 16596-16602.
- 29 D. Shao, L. Shi, L. Yin, B. L. Wang, Z. X. Wang, Y. Q. Zhang and X. Y. Wang, Chem. Sci., 2018, 9, 7986-7991.
- 30 P. Shah and A. D. Westwell, J. Enzyme Inhib. Med. Chem., 2007, 22, 527-540.
- 31 E. P. Gillis, K. J. Eastman, M. D. Hill, D. J. Donnelly and N. A. Meanwell, J. Med. Chem., 2015, 58, 8315–8359.
- 32 N. A. Meanwell, J. Med. Chem., 2018, 61, 5822-5880.
- 33 L. R. Melby, W. Mahler, W. E. Mochel, R. J. Harder, W. R. Hertler and R. E. Benson, J. Am. Chem. Soc., 1962, 84, 3374-3387.
- 34 T. Hasegawa, K. Inukai, S. Kagoshima, T. Sugawara, T. Mochida, S. Sugiura and Y. Iwasa, Synth. Met., 1997, 86, 1801-1802.
- 35 S. A. O'Kane, R. Clerac, H. H. Zhao, O. Y. Xiang, J. R. Galan-Mascaros, R. Heintz and K. R. Dunbar, J. Solid State Chem., 2000, 152, 159-173.
- 36 E. C. Constable, A. J. Edwards, R. Martinezmanez, P. R. Raithby and A. M. W. C. Thompson, J. Chem. Soc., Dalton Trans., 1994, 645-650.
- 37 A. Winter, A. M. J. van den Berg, R. Hoogenboom, G. Kickelbick and U. S. Schubert, Synthesis, 2006, 2873-2878.
- 38 G. M. Sheldrick, Acta Crystallogr., Sect. A: Found. Adv., 2015, **71,** 3–8.

- 39 G. M. Sheldrick, Acta Crystallogr., Sect. A: Found. Adv., 2015, **71**, 3–8.
- 40 O. V. Dolomanov, L. J. Bourhis, R. J. Gildea, J. A. K. Howard and H. Puschmann, J. Appl. Crystallogr., 2009, 42, 339-341.
- 41 F. Neese, WIREs Comput. Mol. Sci., 2012, 2, 73-78.
- 42 F. Weigend and R. Ahlrichs, Phys. Chem. Chem. Phys., 2005, 7, 3297-3305.
- 43 J. M. Tao, J. P. Perdew, V. N. Staroverov and G. E. Scuseria, Phys. Rev. Lett., 2003, 91, 146401.
- 44 V. N. Staroverov, G. E. Scuseria, J. M. Tao and J. P. Perdew, J. Chem. Phys., 2003, 119, 12129-12137.
- 45 A. Schafer, H. Horn and R. Ahlrichs, J. Chem. Phys., 1992, 97, 2571-2577.
- 46 A. Schafer, C. Huber and R. Ahlrichs, J. Chem. Phys., 1994, 100, 5829-5835.
- 47 M. J. Frisch, G. W. Trucks, H. B. Schlegel, G. E. Scuseria, M. A. Robb, J. R. Cheeseman, G. Scalmani, V. Barone, B. Mennucci, G. A. Petersson, H. Nakatsuji, M. Caricato, X. Li, H. P. Hratchian, A. F. Izmaylov, J. Bloino, G. Zheng, J. L. Sonnenberg, M. Hada, M. Ehara, K. Tovota, R. Fukuda, J. Hasegawa, M. Ishida, T. Nakajima, Y. Honda, O. Kitao, H. Nakai, T. Vreven, J. A. Montgomery Jr, J. E. Peralta, F. Ogliaro, M. J. Bearpark, J. Heyd, E. N. Brothers, K. N. Kudin, V. N. Staroverov, R. Kobayashi, J. Normand, K. Raghavachari, A. P. Rendell, J. C. Burant, S. S. Iyengar, J. Tomasi, M. Cossi, N. Rega, N. J. Millam, M. Klene, J. E. Knox, J. B. Cross, V. Bakken, C. Adamo, J. Jaramillo, R. Gomperts, R. E. Stratmann, O. Yazyev, A. J. Austin, R. Cammi, C. Pomelli, J. W. Ochterski, R. L. Martin, K. Morokuma, V. G. Zakrzewski, G. A. Voth, P. Salvador, J. J. Dannenberg, S. Dapprich, A. D. Daniels, O. Farkas, J. B. Foresman, J. V. Ortiz, J. Cioslowski and D. J. Fox, Gaussian, 2013.
- 48 J. D. Chai and M. Head-Gordon, Phys. Chem. Chem. Phys., 2008, 10, 6615-6620.
- 49 X. Zhang, H. Xie, M. Ballesteros-Rivas, Z.-X. Wang and K. R. Dunbar, J. Mater. Chem. C, 2015, 3, 9292-9298.
- 50 M. Llunell, D. Casanova, J. Cirera, P. Alemany and S. Alvarez, SHAPE program, Barcelona, Spain, 2013.
- 51 I. Garcia-Yoldi, J. S. Miller and J. J. Novoa, J. Phys. Chem. A, 2009, 113, 7124-7132.
- 52 R. Ishikawa, S. Ueno, S. Nifuku, Y. Horii, H. Iguchi, Y. Miyazaki, M. Nakano, S. Hayami, S. Kumagai, K. Katoh, Z.-Y. Li, M. Yamashita and S. Kawata, Chem. - Eur. J., 2020, 26, 1278-1285.
- 53 O. Kahn, Molecular magnetism, Wiley-VCH, New York (N.Y.), 1993.
- 54 J. M. Frost, K. L. M. Harriman and M. Murugesu, Chem. Sci., 2016, 7, 2470-2491.
- 55 A. Abragam and B. Bleaney, Electron paramagnetic resonance of transition ions, Clarendon Press, Oxford, 1970.
- 56 K. N. Shrivastava, Phys. Status Solidi B, 1983, 117, 437-458.
- 57 C. M. Klug, A. M. McDaniel, S. R. Fiedler, K. A. Schulte, B. S. Newell and M. P. Shores, Dalton Trans., 2012, 41, 12577-12585.
- 58 J. G. Park, I. R. Jeon and T. D. Harris, Inorg. Chem., 2015, 54, 359-369.

- 59 R. W. Hogue, S. Singh and S. Brooker, *Chem. Soc. Rev.*, 2018, 47, 7303–7338.
- 60 C. P. Slichter and H. G. Drickamer, *J. Chem. Phys.*, 1972, 56, 2142.
- 61 A. B. Gaspar, M. C. Munoz, V. Niel and J. A. Real, *Inorg. Chem.*, 2001, **40**, 9–10.
- 62 S. Gomez-Coca, E. Cremades, N. Aliaga-Alcalde and E. Ruiz, *J. Am. Chem. Soc.*, 2013, **135**, 7010–7018.
- 63 K. A. Schulte, K. R. Vignesh and K. R. Dunbar, *Chem. Sci.*, 2018, **9**, 9018–9026.
- 64 J. Cirera and E. Ruiz, *Comments Inorg. Chem.*, 2019, 39, 216-241.
- 65 S. F. Ye and F. Neese, *Inorg. Chem.*, 2010, 49, 772-774.
- 66 M. Schmidt, D. Wiedemann, B. Moubaraki, N. F. Chilton, K. S. Murray, K. R. Vignesh, G. Rajaraman and A. Grohmann, Eur. J. Inorg. Chem., 2013, 958–967.
- 67 F. Kobayashi, R. Ohtani, M. Nakamura, L. F. Lindoy and S. Hayami, *Inorg. Chem.*, 2019, **58**, 7409–7415.
- 68 R. F. Higgins, B. N. Livesay, T. J. Ozumerzifon, J. P. Joyce, A. K. Rappe and M. P. Shores, *Polyhedron*, 2018, 143, 193–200.
- 69 C. Janiak, *J. Chem. Soc.*, *Dalton Trans.*, 2000, 3885–3896, DOI: 10.1039/b003010o.

- 70 A. I. Anzellotti, C. A. Bayse and N. P. Farrell, *Inorg. Chem.*, 2008, 47, 10425–10431.
- 71 H. J. Wang, H. Y. Xu, W. H. Jia, J. Liu and S. L. Ren, *Energy Fuels*, 2017, **31**, 2488–2495.
- 72 S. Rodriguez-Jimenez, A. S. Barltrop, N. G. White, H. L. C. Feltham and S. Brooker, *Inorg. Chem.*, 2018, 57, 6266–6282.
- 73 A. Bousseksou, J. J. McGarvey, F. Varret, J. A. Real, J. P. Tuchagues, A. C. Dennis and M. L. Boillot, *Chem. Phys. Lett.*, 2000, **318**, 409–416.
- 74 G. Brehm, M. Reiher and S. Schneider, *J. Phys. Chem. A*, 2002, **106**, 12024–12034.
- 75 G. Molnar, V. Niel, A. B. Gaspar, J. A. Real, A. Zwick, A. Bousseksou and J. J. McGarvey, *J. Phys. Chem. B*, 2002, 106, 9701–9707.
- 76 Y. Garcia, H. Paulsen, V. Schunemann, A. X. Trautwein and J. A. Wolny, *Phys. Chem. Chem. Phys.*, 2007, **9**, 1194–1201.
- 77 S. I. Klokishner, M. A. Roman and O. S. Reu, *Inorg. Chem.*, 2011, **50**, 11394–11402.
- 78 D. N. Bowman and E. Jakubikova, *Inorg. Chem.*, 2012, 51, 6011–6019.
- 79 S. Mebs, B. Braun, R. Kositzki, C. Limberg and M. Haumann, Inorg. Chem., 2015, 54, 11606–11624.